Optical Design for Gaussian Beam Elliptical Spot Shaping

&

AOM Double-pass Configuration for Realising Calcium Ion Thermal Qubit

Summer project at Trapped Ion Quantum Information group

Doruk Efe Gökmen[†,‡]

Supervised by

Matteo Marinelli[‡]

Prof. Jonathan Home[‡]

[†] *Department of Physics, Bilkent University*

[‡] *Institute for Quantum Electronics, ETH Zürich*

Zurich, September 5, 2017

Abstract The study of optimisation and modulation of optical fields generated by the laser sources is crucial in quantum information processing (QIP) with trapped ions to obtain more effective cooling mechanisms and to increase the fidelity of the logical gates that are implemented. The current optical setup at the Trapped Ion Quantum Information (TIQI) group has limited ability in addressing long chains of ions with high efficiency in 3D segmented trap experiments. To achieve a more efficient way of addressing chains of ions by generating an elliptical beam spot whose major axis is aligned along the trap axis, an afocal optical system consisting of cylindrical lenses is designed and assembled. The first chapter of this thesis describes the design and presents the results of assessments on the setup. It has been verified that the assembled setup is able to produce two types of focused elliptical beam spots, one with and aspect ratio 2 and the other with 4. Ultimately, this setup is expected to both increase the fidelity in the current protocols and allow future experiments with longer chains of ions which might include quantum simulation of spin systems.

The topic of the second chapter of this thesis is the AOM design that is built towards the aim of realising a micro-thermodynamics experiment that is proposed by Prof. R. Renner's group in ETH. The proposal suggests a prospect of realisation of Szilard's engine using trapped beryllium and calcium ions. The current setup is able to access all of the relevant transitions suggested in the protocol, except for $|^2S_{1/2}, m_J = -1/2\rangle \leftrightarrow |^2D_{5/2}, m_J = -1/2\rangle$ transition in calcium. The required transition frequency for this is achieved by first, locking the 729 nm laser to the lower fringe to reduce the frequency one free spectral range of 1.5 GHz and then, using an 200 MHz AOM in double-pass configuration to increase the frequency by 400 MHz. Decent efficiency in the AOM setup is achieved. Accessing the mentioned calcium transition through the work presented here is an important step towards realising the proposed experiment.

Contents

0.1 Introduction

The following thesis reports on the three months of research performed in the ETH Zürich Trapped Ion Quantum Information (TIQI) group. The research is concerned with the 3D segmented trap experiment in TIQI group. Work involved designing two different setups for independent purposes, purchase of the components and assembling the two setups along with the first measurements regarding performance tests.

Two parts of the project are discussed separately in its respective chapter. In each two chapters, I mainly discuss the design, construction and equipment details after providing a concise theoretical grounding for the principles of operation and motivating the work that is done. Measurements regarding the performance assessments are given towards the end of each part of the thesis.

Chapter 1

Optical System for Generating Elliptical Beam Spots

In the first part of the project, a compact optical system that generates elliptical beams is designed and constructed. Ability to use an elliptical beam whose major axis is oriented along the trap axis will allow to address longer chains of ions, faster gates and better beam pointing stability, hence higher fidelity in the future experiments that are going to be performed by the TIQI group.

In the most basic sense, the design consists of an afocal system with cylindrical lenses that magnifies the incident collimated spherical Gaussian beam at different rates in the two axes, so that the output collimated beam has an elliptical Gaussian intensity profile according to this mismatch in the magnification in two axes. This collimated beam can be tuned by the afocal system to attain specific properties so that when it is focused, the beam spot has the desired aspect ratio. The aspect ratio of the focused elliptical beam can be adjusted to be 2 or 4 by using an adjustable Cooke triplet in the trap axis.

1.1 Background

As a result of widespread intensive study over the last few decades, cold atomic ions in electrodynamic traps are now considered to be one of the most promising approaches for constructing a scalable universal quantum computer [1]. Optical fields have a wide range of application in the field of quantum information processing (QIP) with trapped ions, e.g. laser cooling, initalising the electron energy levels and manipulation of the transitions for logic gates [2]. Hence, it is clear that the study of optimisation and modulation of these optical fields generated by the laser sources is crucial in QIP to obtain more effective cooling mechanisms and to increase the fidelity of the logical gates that are implemented.

Ions in Paul traps Due to its electric charge, one needs to create an electrodynamic potential well to trap an ion. A well established method is the Paul trap [3], which uses DC and RF fields to create the well.

Harmonically trapped ions are described by their electronic (internal) states $\{|\uparrow\rangle, |\downarrow\rangle\}$ and vibrational (motional) states $\{|n\rangle\}$. In addition, when a trapped ion interacts with light, it is described by the following Hamiltonian in the interaction picture.

$$H = H_0 + \frac{\hbar}{2}\Omega \left\{\exp\left[i\eta(\hat{a}e^{-i\omega_z t} + \hat{a}^\dagger e^{i\omega_z t})\right]\hat{\sigma}^+ e^{-i\Delta t} + \text{H.C.}\right\} \tag{1.1}$$

where Δ is the laser-atom detuning; $\hat{\sigma}^\pm$ are the internal raising and lowering operators whilst $\hat{a}$ and $\hat{a}^\dagger$ denote the creation or annihilation operators for motional quantum, respectively. Note that this expression is valid under the rotating wave approximation.

In the Lamb-Dicke regime, and under a second rotating wave approximation, (1) reduces into a simpler form. Then it can easily be seen that for $\Delta = 0$ the Hamiltonian describes a carrier transition that couples $|\downarrow, n\rangle$ with $|\uparrow, n\rangle$ and for $\Delta = \pm\omega_z$, (+) describes the blue sideband transition which couples $|\downarrow, n\rangle$ with $|\uparrow, n-1\rangle$ and (−) describes the red sideband transition which couples $|\downarrow, n\rangle$ with $|\uparrow, n+1\rangle$. A derivation is omitted in regards of the scope of this paper, details can be found in ref. [4]. This coupling of motional and internal states permits sideband cooling of ions [5] and implementation of quantum gates [6].

1.1.1 QIP with Chains of Ions

Chains of trapped ions has advantages in certain applications of QIP. Apart from allowing to achieve faster quantum logic gates, one of the most promising prospects of these systems is in quantum simulation. As an example, these laser cooled and trapped ion chains constitute an ideal system for the simulation of interacting quantum spin models. The effective spins are represented by appropriate internal energy levels of an ion, and a high efficiency measurement of the spins is possible using state-dependent fluorescence techniques [7].

Aside from quantum simulation, recently, there has been rapid development on the control and manipulation of the quantum states of trapped ions in ion chains that contain multiple ion species [8].

Chains of mixed ion species for QIP

Advantages of using hybrid systems consisting of chains of mixed ions species is twofold. Firstly, one can exploit the extra degrees of freedom introduced by different species to expand and refine the control of the system by delegating specific tasks to the most suitable subsystem [9, 10]. Secondly, using arrays of multiple species permit sympathetic cooling for state preparation. Although most ion species are difficult to laser cool, it has been demonstrated that one can partially overcome this limitation by using sympathetic cooling on arrays of two ion species [11].

Sympathetic cooling In sympathetic cooling, one species is cooled by interaction with a second directly cooled species [12]. Ions that are difficult to cool directly are cooled by collisional coupling with other stored ions which are easier to cool. Furthermore, in previous experiments at NIST [13] it has been showed that the level structure of the sympathetically cooled species is not perturbed seriously since the radiation that is used to directly cool the refrigerant species is far from any resonance in sympathetically cooled species.

At the ETH segmented trap setup, $^{40}Ca^{+}$ ion is used as the refrigerant species to sympathetically cool $^{9}Be^{+}$ ions. An advantage in using $^{40}Ca^{+}$ is that all relevant transitions, e.g. 729 nm and 397 nm, can be addressed by diode lasers without the need of complicated optics. On the other hand, the $^{9}Be^{+}$ qubit is usually opted for its lower mass hence allowing higher trap frequencies to be used. $^{9}Be^{+}$ has also a first order magnetic field insensitive transition which show coherence times of seconds.

1.1.2 Focused Gaussian Beams

In designing the optics, a geometrical optics treatment suffices for determining the focal lengths and separation of the lenses that generate *collimated* elliptical beam with a given aspect ratio. On the other hand, in order to get the desired beam waist in both dimensions for the *focused* beam, one needs to take physical optics into account. Therefore in this section, the general properties of Gaussian beams and characteristics of Gaussian beams that pass through a train of lenses are described by a formalism that comprises both physical optics and certain strengths of geometric optics.

General properties of Gaussian beams

A laser beam is usually described by a Gaussian profile. An ideal Gaussian beam has a transverse electric field and and intensity distribution described by a Gaussian function. These Gaussian modes are the solution of the so called paraxial wave equation that is obtained by making the paraxial approximation to the Helmholtz equation for the electromagnetic field.

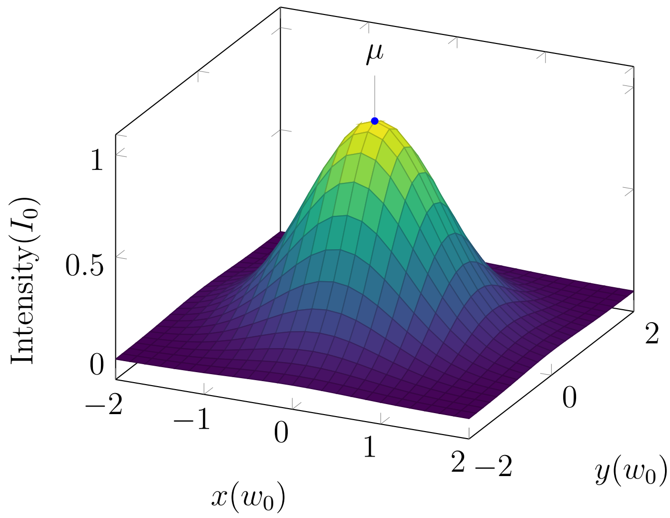

Figure 1.1: The intensity profile of a spherical Gaussian beam.

In cylindrical coordinates (s, θ, z) specific solution to this equation is given by the field

$$E(s, z) = E_0 \frac{w_0}{w(z)} \exp\left(-\frac{s^2}{w^2(z)}\right) \exp\left(-ig(s, z)\right) \tag{1.2}$$

The beam waist $w_0 = w(z_0)$ is defined as the minimum value of the beam width $w(z)$ and $g(z)$ is the Gouy phase. For a purely real $g(z)$ function, the corresponding optical intensity profile function reads

$$I(s, z) = \frac{c\epsilon_0}{2} |E(s, z)|^2 = I_0 \left(\frac{w_0}{w(z)}\right)^2 \exp\left(-\frac{2s^2}{w^2(z)}\right) \tag{1.3}$$

which is plotted in Figure 1.1.

The transverse extent of this propagating electromagnetic field is described by the *beam width* function:

$$w(z) = w_0 \sqrt{1 + \left(\frac{z}{z_R}\right)^2} \tag{1.4}$$

whose curvature depends on the parameter z_R which is called the *Rayleigh range*.

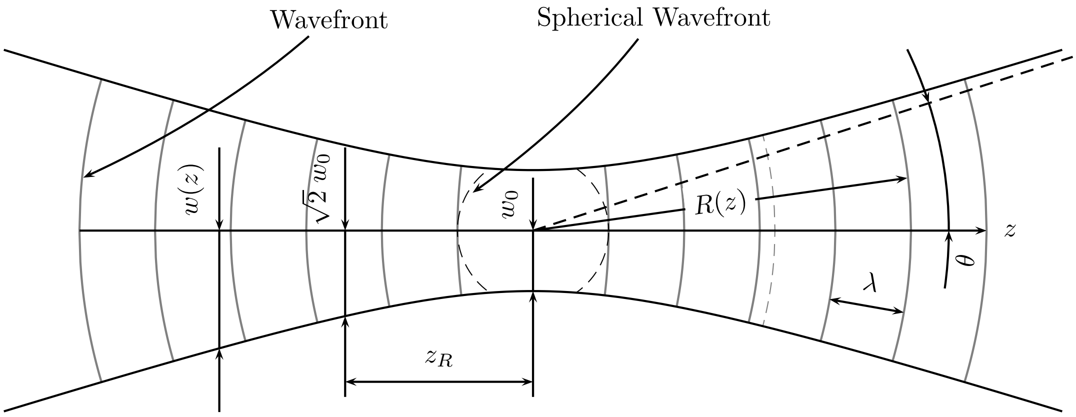

Figure 1.2: Illustration and main characteristics of a spherical Gaussian beam. The surfaces of constant field strength form a hyperboloid along the z axis.

z_R is defined for a Gaussian mode with wavelength λ as

$$z_R = \frac{\pi w_0^2}{\lambda} \tag{1.5}$$

Using this parameter, one can define the radius of curvature as

$$R(z) = z + \frac{z_R^2}{z}. \tag{1.6}$$

This indicates that within the Rayleigh range, the radius of curvature is minimum, resembling a spherical wave; whereas outside the Rayleigh range, the curvature gets unboundedly larger with increasing z, ultimately converging to a plane wave. This reflects the fact that the Gaussian beams carry properties of both plane and Gaussian waves. The beam width function $w(z)$ given in equation 1.4 is plotted in Figure 1.2 along with these important parameters that are mentioned.

There are important differences between conventional uniform spherical beams and Gaussian beams in terms of the effects of lenses. Firstly, when the waist of the incident beam is at the front focal plane of a convex lens, the lens generates a beam that has waist at the back focal plane, instead of a collimated beam as would have been predicted by geometric optics [14]. Another difference is that the position of the image waist for a Gaussian beam alters from its geometric optics position [15].

Effect of lenses on Gaussian beams The transformation of a Gaussian beam under the action of lenses can be studied using a matrix algebra formalism. This formalism is invented by S. A. Self in 1976 [14] and it involves introducing physical optics parameters w_0 and z_R that explain Gaussian beams to the formulas of geometric optics. z_R is simply recalculated at each step of a transformation by a lens.

In the following part of this section, the transformation of the beam waist for the Gaussian beam that passes through a lens with focal length f is calculated. Note the convention that the unprimed parameters ξ belong to the beam incident to the lens, and the primed parameters ξ' belong to the emerging beam.

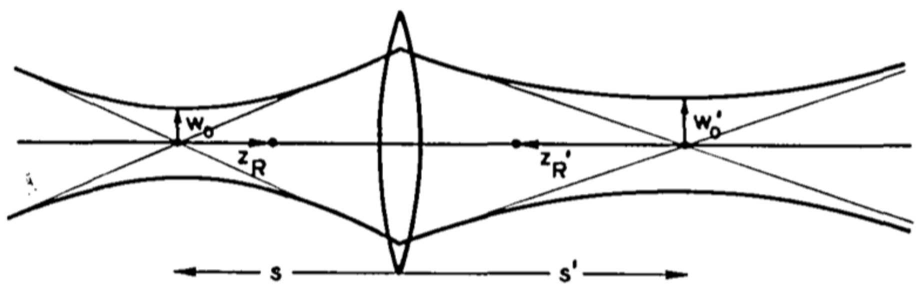

Figure 1.3: Geometry of the imaging of a Gaussian beam by a converging lens and real object and image waists. Figure retrieved from [14].

Let us regard the waist w_0 of the incident beam as the object placed a distance s away from the lens, and the waist w_0' of the emerging beam as the image placed s' away from the lens (see Figure 1.3). We are after an expression of the emerging beam in terms of the parameters of the incident Gaussian beam and the focal length of the lens. That is, the question is what $w_0'(w_0, s, f)$ is.

To proceed in applying Self's formalism, it is first assumed that the lens can be approximated by a thin lens. This implies that, if we place the origin at the position of the waist for both the incident and the emerging beam, i.e. $w(z = 0) = w_0$ and $w'(z' = 0) = w_0'$, then $w(s) = w'(s')$ since the beam width at each point has to be uniquely defined. Introducing the parameter $\beta \equiv \frac{\pi w_0^2}{\lambda s}$ and $\beta' \equiv \frac{\pi {w_0'}^2}{\lambda s'}$ allows us to take advantage of this condition. Using equations 1.4 and 1.5 for expressing the beam widths in terms of β and β', we get that

$$w_0 \left[1+\frac{1}{\beta^2}\right] = w_0' \left[1+\frac{1}{\beta'^2}\right]; \tag{1.7}$$

and similarly using equation 1.6 for the radius of curvature, we obtain

$$R(s) = s'[1+\beta^2], R'(s') = s'[1+\beta'^2]. \tag{1.8}$$

By combining equations (1.7) and (1.8) it is obtained that

$$\frac{w_0^2}{w_0'^2} = \frac{s}{s'}\frac{R(s)}{R'(s')}. \tag{1.9}$$

Further, for a thin lens, the reciprocal of the radius of curvature changes by an amount $\frac{1}{f}$ as the beam passes through:

$$\frac{1}{R'(s')} = \frac{1}{R(s)} - \frac{1}{f} \implies R'(s) = \frac{fR(s)}{f-R(s)}. \tag{1.10}$$

Therefore if we substitute this expression of $R'(s)$, then equation (1.9) can be expressed as

$$\frac{w_0^2}{w_0'^2} = \frac{s}{s'}\frac{f-R(s)}{f}. \tag{1.11}$$

To eliminate the remaining s' parameter in this relation, using the fact that $w(s) = w'(s')$ we can indeed express s' itself in terms of s which reads $s' = \frac{\pi w_0'}{\lambda}\sqrt{w^2(s) - w_0'^2}$. Substituting this in equation (1.11) yields

$$\frac{\pi w_0^2}{\lambda}\sqrt{\left(\frac{w(s)}{w_0'}\right)^2 - 1} = s\left(\frac{f-R(s)}{f}\right). \tag{1.12}$$

Then we can simply extract w_0' and attain the expression for the beam waist of the emerging beam that we are after

$$w_0'(w_0, s, f) = \frac{w(s)}{\sqrt{1+\left[\frac{\lambda s}{\pi {w_0}^2}\left(\frac{f-R(s)}{f}\right)\right]^2}}. \tag{1.13}$$

Lastly, observing that $\frac{\lambda s}{\pi w_0^2} = \frac{s}{z_R}$, and substituting the radius of curvature from equation (1.6) and the beam width from equation (1.4) we get the explicit relationship,

$$w_0'(w_0, s, f) = w_0\sqrt{\frac{1+\left(\frac{s}{z_R}\right)^2}{1+\left(\frac{s}{z_R}\right)^2\left(\frac{f-s-z_R^2/s}{f}\right)^2}}. \tag{1.14}$$

This equation have been used in determining the focal lengths of the lenses and the separation between them in the afocal system that is necessary for obtaining a focused beam spot with a given beam waist.

1.2 Setup: Elliptical Beam Telescope

In this section, the design of the optical system is described. The properties of the incident and the desired output beams, and the required values for the main parameters corresponding to the optics are presented.

Properties of the incident beam and the desired output beam The 313nm incident collimated beam that is received by the optical system is a spherical Gaussian mode with beam-radius of 300µm. The current focusing optical system is able to attain a beam spot of radius 20µm at focal. This spot size is convenient for the $^{9}Be^{+}$ - $^{40}Ca^{+}$ - $^{9}Be^{+}$ ion chain aligned in the trap axis with an inter-ion spacing of 5µm. However considering that the spot is circular, a significant amount of power is wasted due to the vertical extent of the beam where no ion lives. Furthermore, in the future experiments, if chains of more than 3 ions are loaded in the trap, it would not be possible to address the whole chain with the current optical setup which is not adjustable for larger spot sizes.

Using a beam with an elliptical spot shape whose major axis is parallel to the trap axis is feasible for solving both of these issues. Furthermore, an adjustable compact optical design paves the way for performing different types of experiments with single ions or chains of ions with the current experimental setup. Therefore, two types of elliptical spots corresponding to each type of experiment are determined beforehand. The sizes of these are given in terms of beam width $w^i(z)$ along horizontal $(i = h)$ and vertical $(i = v)$ axes, in Table 1.1 and the corresponding beam spots are depicted in Figure 1.4.

Incident Beam	Type 1 Focused	Type 2 Focused
$w^h = 300\mu m$	$w^h = w_0^h = 20\mu m$	$w^h = w_0^h = 40\mu m$
$w^v = 300\mu m$	$w^v = w_0^v = 10\mu m$	$w^v = w_0^v = 10\mu m$

Table 1.1: Values for the desired spot sizes of the focused beam

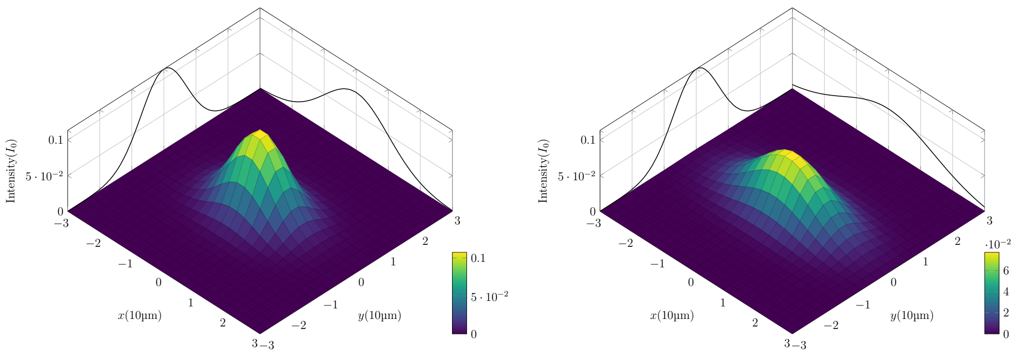

Figure 1.4: The intensity profiles of the desired focused beam spots. Left: Type 1, right: Type 2.

The first type of beam presented in Table 1.1 has an elliptical spot with aspect ratio $\frac{w^h}{w^v} = 2$ which is convenient for experiments where there are chains of 3 or less trapped ions. The Type 2 has an aspect ratio of $\frac{w^h}{w^v} = 4$ to be utilized in experiments with longer chains of up to 7 ions.

Note that the spot sizes given in Table 1.1 are for a beam focused by a spherical lens with a focal length of 20cm (see the lens labeled "spherical" in figures 4 and 5). Using the formalism in Section 1.2.2, one can determine the necessary dimensions of the collimated beam spot for obtaining each type of focused spots. It has been calculated that the collimated elliptical beams that is generated by the optical system should have an aspect ratio of $\frac{w^h}{w^v} = 0.5$ for the Type 1 focused spot and $\frac{w^h}{w^v} = 0.25$ for the Type 2 focused spot.

The beam width for the collimated beams corresponding to each type of focused spot are given in Table 1.2. Moreover, the spot shapes are presented in Figure 1.5.

Type 1 Collimated	Type 2 Collimated
$w^h = 900\mu m$	$w^h = 450\mu m$
$w^v = 1800\mu m$	$w^v = 1800\mu m$

Table 1.2: Values for the desired spot sizes of the collimated beam

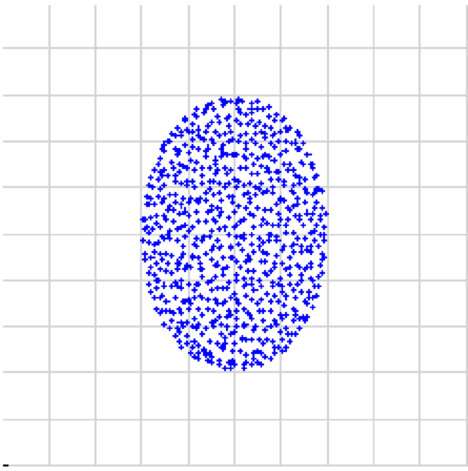

(a) The shape of the collimated beam with an aspect ratio of $\frac{w^h}{w^v} = 0.5$ for generating Type 1 focused spot.

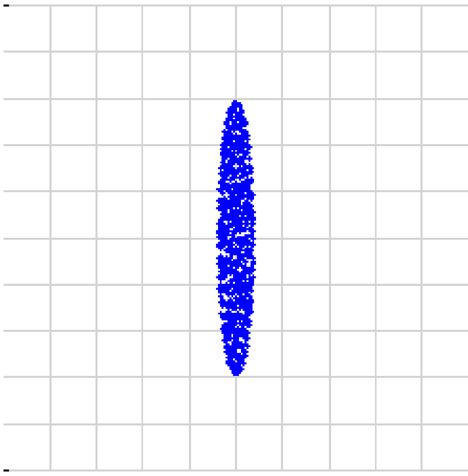

(b) The shape of the collimated beam with an aspect ratio of $\frac{w^h}{w^v} = 0.25$ for generating Type 2 focused spot.

Figure 1.5: The spot shapes of the collimated beam that correspond to (a) the focused beam with aspect ratio $\frac{w^h}{w^v} = 2$ (Type 1) and (b) the focused beam with aspect ratio $\frac{w^h}{w^v} = 4$ (Type 2).

1.2.1 Optical Design

The optical design consists of two telescopes for magnifying the incident collimated beam at different rates along the horizontal and the vertical axes. The afocal system generates a collimated elliptical beam. This beam is focused by a final $f = 20$cm spherical lens. Note that from now on, the horizontal axis is referred to as the trap axis.

General description of the setup To get as small beam widths as indicated in Table 1.1, one needs to magnify the collimated beam in both axes before focusing. Furthermore, the cylindrical lenses have independent effects on the horizontal and the vertical components of the incident beam profile. Therefore the consequent parts of the optical system which exclusively correspond to each axes can be considered separately.

In the vertical axis, since the magnification is fixed, a simple Galilean Telescope is implemented using vertically aligned cylindrical lenses. For the trap axis, since the system has to be adjustable to easily switch between two configurations (see Figure 1.2), a Cooke triplet is implemented by using horizontally aligned cylindrical lenses that can be slid. The whole optical setup is assembled using a cage system.

Galilean Telescope for the Vertical Axis

Comparing the w^v value of the incident beam given in Table 1.1 and the w^v value for the collimated beam given in Table 1.2, it can be seen that the magnification required magnification factor in the vertical axis is 6. This is achieved using cylindrical lenses with focal lengths $f_1^v = -12.7$mm and $f_2^v = 75$mm which are denoted by Y_1 and Y_2 (see Table 1.3) in Figure 1.6, respectively. By ray tracing, it can be seen that the the distance between the lenses Y_1 and Y_2 is simply $d_1 = f_2^v - f_1^v = 6.23$cm.

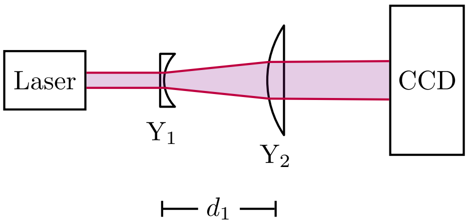

Figure 1.6: The portion of the optical system which magnifies the beam along the vertical axis is operationally equivalent to a Galilean telescope.

Cooke triplet for the trap axis

To obtain an adjustable beam width, it was necessary to deploy a variation of photographic zoom lens using horizontally oriented cylindrical lenses. Although there are many possible designs for zoom lenses, the most complex ones having upwards of thirty individual lens elements and multiple moving parts, the most basic one of these is a Cooke triplet which was invented by Dennis Taylor of the company T. Cooke & Sons. Therefore the part of the design that magnifies the beam along the trap axis (Figure 1.8) is inspired by Taylor's Cooke triplet design [16].

Another advantage of the Cooke triplet is that it allows elimination of most of the optical aberration at the outer edge of the lenses. It has the feature of having the smallest number of elements that can correct all Seidel aberrations.

How Cooke triplet works A Cooke triplet comprises a concave element in the centre with a convex element on each side. The convex lenses are of equal focal length. In order to be able to generate collimated light with both maximum magnification and de-magnification, the concave element in the centre has to have an absolute focal length less than half of the convex lenses, i.e. $f_2 < f_1 = f_3$ (see Figure 1.7). As it is indicated in Figure 1.7, when varying the overall magnification of the system, the lens L_3 is fixed and lenses L_1 and L_2 are axially translated in a specific nonlinear relationship.

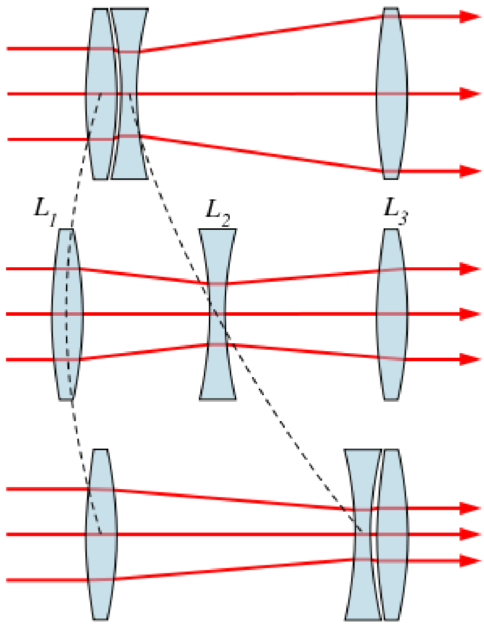

Figure 1.7: Cooke triplet in three different configurations; (1): magnify, (2): ineffective, (3): de-magnify.

Comparing incident beam width with the first row of Table 1.2, one can deduce that the magnification factors that are required from the afocal system are 3 and 1.5 for the type 1 and type 2 focused spots, respectively. This is achieved by using lenses X_1 as L_2 and X_2 as L_1 (see Table 1.3)[1]. Furthermore, the separation between the lenses d_2 and d_3 (see Figures 8 and 10) to obtain each type of focused spot is given in Table 1.4.

The focal length of the whole set of lenses that are used in the optical setup are given in Table 1.3. Note that X_j is the same lens as Y_j with the only difference that the former is aligned perpendicular with respect to the latter.

[1]These lenses are retrieved from Thorlabs, Inc. with model numbers: X_1,Y_1: LK4155-UV and X_2, Y_2: LJ4878-UV.

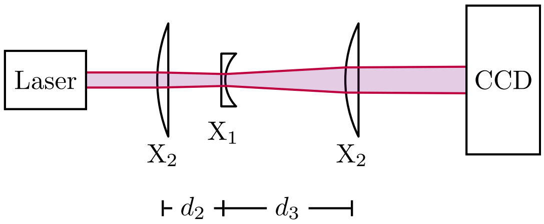

Figure 1.8: It is possible to obtain focused beam profiles with two different aspect ratios, namely 2 and 4, by using two different configurations of the Cooke triplet which consists of three cylindrical lenses oriented along the trap axis. See Table 1.4 for the values.

X$_1$	$f_1^h = -12.7$mm	$f_1^v = \infty$
X$_2$	$f_1^h = 75$mm	$f_1^v = \infty$
Y$_1$	$f_1^h = \infty$	$f_1^v = -12.7$mm
Y$_2$	$f_1^h = \infty$	$f_1^v = 75$mm
Spherical	$f_1^h = 200$mm	$f_1^v = 200$mm

Table 1.3: The lens types that are used

The schematic representation of the full setup is given in Figure 1.9 and Figure 1.10. As it can be seen there, the Galilean telescope and the Cooke triplet are assembled in a way that two sections are placed one within another. This allows to compactify the design. In the final assembly with a cage system, the first two lenses depicted in Figure 1.9 and 1.10 are free to be translated while the others are fixed. The overall length of the system is about 20cm [2].

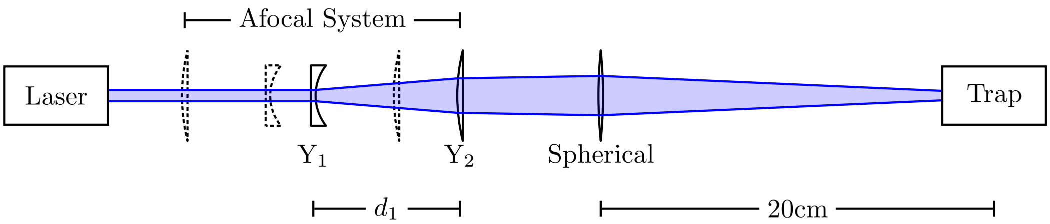

Figure 1.9: The full setup viewed from the vertical axis. The dotted lenses are effective along the horizontal direction.

[2]Please note that the high curvature due to the small radius of the concave lens causes distortion when the curved face points towards the incident beam. For this reason, in the optical system the flat faces of the both concave lenses point towards the incident beam.

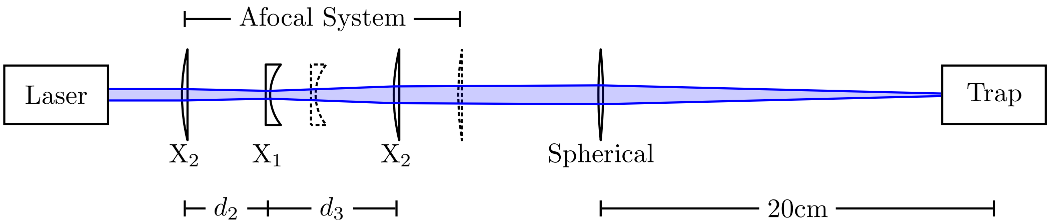

Figure 1.10: The full setup viewed from the trap axis. The dotted lenses are effective along the vertical direction.

	d_1	d_2	d_3
Type 1	6.23cm	2cm	5.5cm
Type 2	6.23cm	3cm	5.2cm

Table 1.4: The required lens separations in the optical system for obtaining type 1 and type 2 focal beam spot.

1.3 Back-reflector

This section discusses the back-reflector design which is placed after the afocal system with the focusing lens that has been discussed, so that the ion trap is positioned in between. Using the back-reflector has two advantages. Firstly, in case of a shift of the focal position for the focused elliptical beam due to a misalignment of lenses in the afocal optical system, replaces the focal position onto the ion trap. Secondly, using the reflected light allows us to address radial modes of $^9Be^+$.

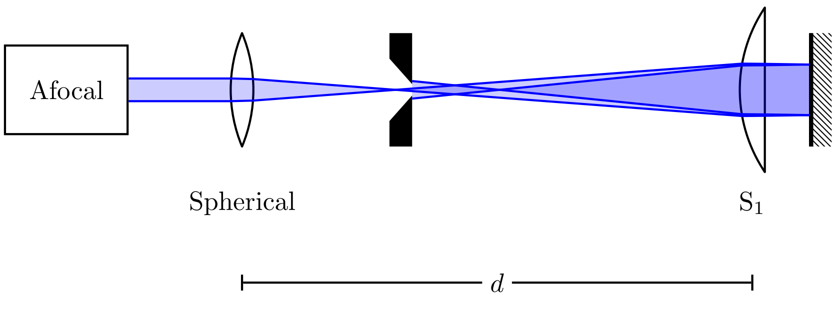

Figure 1.11: The schematic of the back-reflector. In case of a misalignment of lenses in the afocal system, the back-reflector corrects the shift in the position of the focal point. Note that this figure is not to scale.

A primitive design for the back-reflector is given in Figure 1.11. It has been determined in the optical design software Zemax, that by using a spherical lens S_1 of focal length $f = 2.5$cm, and the parameter $d \approx$25cm (see Figure 1.11), it has been possible to tune the focal position within a range of about 1cm. Although a significant misalignment of lenses in the afocal setup may cause shifts that are larger than 1cm, a range of 1cm is supposed to be convenient in case of a careful alignment.

1.4 Setup Characterization

In this section, results of the tests that the system was subjected to are presented. It has been verified that the system generates the desired beam spots by performing knife edge measurements on the intensity profile. Furthermore, the power efficiency of the system is presented towards the end of this section.

1.4.1 Beam profile

The intensity profile of the beam is measured both right after the afocal optical system (see Figure 1.12.a and Figure 1.13.a) and after being focused (see Figure 1.12.b and Figure 1.13.b). The method is that, the total optical power in the beam spot is recorded as a knife edge is translated through the spot using a calibrated translation stage. The power meter records the integral of the Gaussian beam intensity between $-\infty$ and the position of the knife. Hence, for a Gaussian profile, the measurement yields the corresponding *complementary error function*

$$\mathrm{erfc}(x) = \frac{1}{\sqrt{2\pi\sigma^2}} \int_{-\infty}^{x} e^{\frac{-t^2}{2\sigma^2}}\, \mathrm{d}t. \tag{1.15}$$

The intensity profile is obtained by performing numerical differentiation to the measurement data. Furthermore, the position of the beam waist is determined by performing 3 measurements of the beam width within the Rayleigh range, fitting the function for the beam width $w(z) = w_0\sqrt{1 + \left(\frac{z}{z_0}\right)^2}$ (equation 1.4) to this data. The beam waist is the minimum value of the function that is fitted. The measurement results for the focused beam profile are given in Table 1.5.

Type 1 Focused	Type 2 Focused
$w^h = 26\mu\text{m}$	$w^h = 45.832\mu\text{m}$
$w^v = 12.84\mu\text{m}$	$w^v = 10.83\mu\text{m}$

Table 1.5: Measured values for the focused beam widths

A comparison between the Tables 1 and 5 indicates that the measured values match the intended values reasonably well. The error is mainly due to the fluctuations in the optical power that the M Squared laser that is used to test the setup. These focused intensity profiles are presented Figures 1.12.b and 1.13.b. The Figures 1.12.a and 1.13.a are the intensity profiles of the beam right after the afocal optical system.

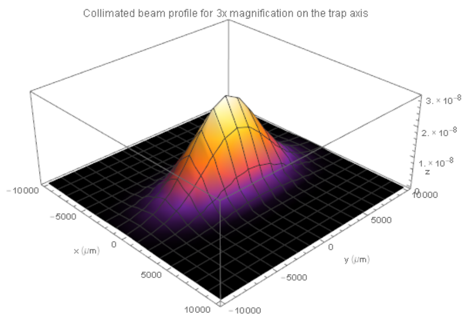

(a) The measured intensity profile of the collimated beam with an aspect ratio of $\frac{w_0^h}{w_0^v} = 0.48$.

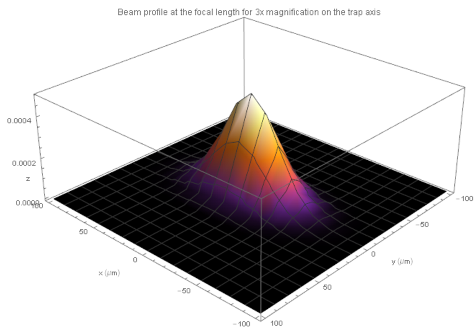

(b) The measured intensity profile of the focused beam with an aspect ratio of $\frac{w_0^h}{w_0^v} = 2.02$.

Figure 1.12: The intensity profiles of the collimated (a) and the focused (b) beams generated by the optical system in the Type 1 configuration. Note the different scales in (a) and (b).

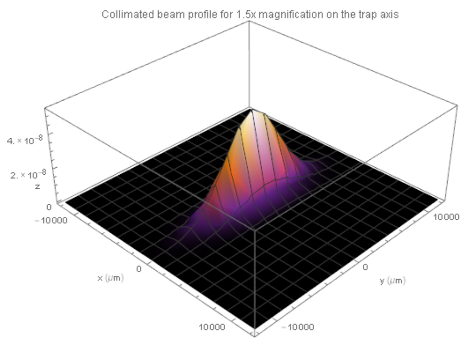

(a) The measured intensity profile of the collimated beam with an aspect ratio of $\frac{w_0^h}{w_0^v} = 0.26$.

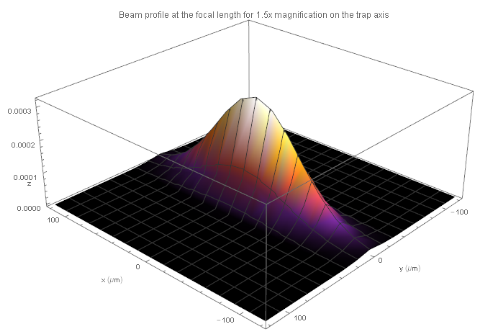

(b) The measured intensity profile of the focused beam with an aspect ratio of $\frac{w_0^h}{w_0^v} = 4.5$.

Figure 1.13: The intensity profiles of the collimated (a) and the focused (b) beams generated by the optical system in the Type 2 configuration. Note the different scales in (a) and (b).

1.4.2 Efficiency

According to the Thorlabs Inc. website, the UV fused silica lenses that are used in the optical setup have a transmission rate[3] of $T = 93.053\%$ for 313 nm light [17]. Therefore for the afocal optical system that comprises 5 of these lenses, the optical transmission efficiency is $T^5 \simeq 70\%$.

1.5 Conclusion

This chapter of the thesis describes the design of the afocal optical system that is used for elliptical beam spot shaping. Two types of focused beam spots have been achieved. For both types, the focused beam spot has an extent of about 10μm in the vertical axis. Type 1 has an aspect ratio of ≈2 between horizontal and vertical dimensions. It has been verified that the extent about 20μm of the focused spot in the trap axis for an incident collimated beam of radius 300μm. This is useful for single ion experiments with sympathetic cooling. Type 2 has an aspect ratio ≈4, which has also been verified to have an extent of 40μm in the trap axis, which is useful for addressing ion chains of more than 7 ions.

A back-reflector design is made. In case of a misalignment of the lenses in the afocal system, the back-reflecting setup corrects the shifts in the focal

[3]Measured for a 10 mm thick sample.

position if the shift is less than 1 cm. Furthermore, the opposite momentum direction of the back-reflected light allows us to address the radial modes of $^9Be^+$.

More work remains. The presented back-reflector design has not been tested yet. However it is evident that since it comprises a single spherical lens instead of cylindrical lenses, it causes some distortion in the elliptical beam shape that is generated by the afocal system. If a test on the system indicates that this effect is significant, then the back-reflector design will have to be modified with cylindrical lenses.

The afocal assembly for elliptical beam spot generation promises addressing longer chains of ions with power efficiency. In addition, although the back-reflector is still to be tested, we are close to being able to address the radial modes of $^9Be^+$.

Chapter 2

AOM Setup for Realising Calcium Ion Thermal Qubit

The second part of my project involved designing and assembling an AOM setup for addressing the $|^2S_{1/2}, m_J = -1/2\rangle \leftrightarrow |^2D_{5/2}, m_J = -1/2\rangle$ transition in $^{40}Ca^+$ ions. Accessing this transition is an important step important to realise a micro-thermodynamics experiment[1] that is concerned with work extraction from the trapped ions by converting information contained by the trapped ion into a thermal distribution.

The transition frequency is achieved by including an extra optical setup with 200 MHz frequency AOM in the *double-pass configuration* to the current experimental setup. The design breadboard with an double-passing AOM is done. The setup is assembled and then the alignment of the optical components is adjusted so that the efficiency for the +1 order diffraction taken from the AOM is maximised.

2.1 Background

The goal of the thermodynamics experiment that is proposed by the Renner group is to implement a state independent work extraction gate that explicitly stores the extracted work with trapped ions.

There are 3 elementary thermodynamic units that are necessary for converting quantum information into work. These are namely, a battery I of information qubits, a thermal bath Q modelled as an arbitrary number of qubits in the Gibbs state at fixed temperature, and a work storage system W. The protocol involves using the information of one initially pure ground

[1]Proposal belongs to Prof. R. Renner's Quantum Information Theory group at ETH Zürich.

state I qubit to convert heat from the coupled thermal bath Q initially in a thermal distribution into work stored in W. The unitary action that is sought, extracts work by converting information in initial pure state of I into a classical statistical ensemble of the elements of the set $\{|1\rangle_I, |0\rangle_I\}$ whilst the heat bath ends up in the almost pure ground state $|0\rangle_Q$.

A Szilard engine? Entropy quantifies the degree of ignorance about the state of the system. Furthermore, due to the second law of thermodynamics, energy contained in a system can be entirely converted to work only if the microstate, i.e. complete information about the system is available at a cost of that information. According to Landauer's Principle, erasure of one bit of information is accompanied by at least $k_B T \ln 2$ of heat, hence one can in principle use one bit of information to extract a work $W = k_B T \ln 2$.

Because of the fact that the protocol which is the subject of this work makes it possible to analyse the microscopic changes during a thermodynamic process that generates work through an increase of information entropy, the proposed experimental scheme makes it possible to realise an *ionic Maxwell's demon* experiment by building a Szilard's engine, in other words, it provides a test for the Landauer erasure principle.

The implementation of this scheme with atomic physics, in particular with ions, is possible by using $^9\mathrm{Be}^+$ as the information battery qubit and $^{40}\mathrm{Ca}^+$ as the thermal qubit. The reason for this choice is the ability of $^{40}\mathrm{Ca}^+$ to undergo fast adiabatic passages. The relevant transitions in $^9\mathrm{Be}^+$ are currently accessible with the current setup, and therefore, as indicated before, this work is concerned with $^{40}\mathrm{Ca}^+$.

2.1.1 Calcium Ion

Energy levels The internal level structure of $^{40}\mathrm{Ca}^+$ is given in Figure 2.1 with the relevant transitions. For an ion placed in a magnetic field, the state $^2S_{1/2}$ splits into two levels and the state $^2D_{5/2}$ splits into six levels due to Zeeman effect. For our thermal qubit, we address the $|^2S_{1/2}, m_J = +1/2\rangle \leftrightarrow |^2D_{5/2}, m_J = -1/2\rangle$ and $|^2S_{1/2}, m_J = -1/2\rangle \leftrightarrow |^2D_{5/2}, m_J = -1/2\rangle$ transitions with respective frequencies ω_1 and ω_2 which approximately correspond to a wavelength of 729 nm.

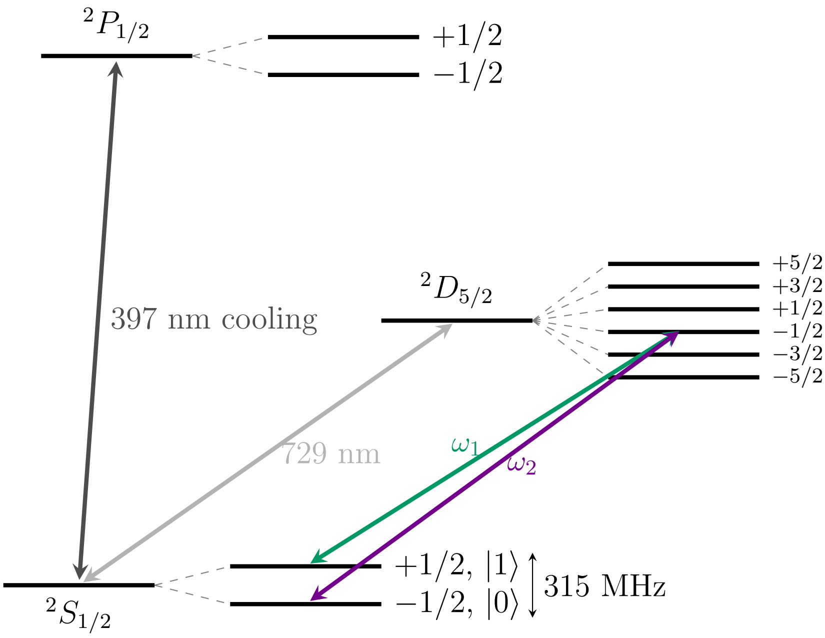

Figure 2.1: $^{40}Ca^+$ energy level diagram with the relevant transitions drawn. The transition that is to be addressed with the AOM setup is indicated by purple colour.

The thermal qubit states are $|0\rangle = |^2S_{1/2}, m_J = -1/2\rangle$ and $|1\rangle = |^2S_{1/2}, m_J = +1/2\rangle$. The two transitions of frequencies ω_1 and ω_2 couple the qubit states $|0\rangle$ and $|1\rangle$ hence they are necessary to perform the protocol and use calcium as the thermal qubit. The long lifetime of about 1.1 seconds for the $^2D_{5/2}$ manifold make these transitions feasible for quantum manipulation [18]. On the other hand, note that the ω_1 transition has $|\Delta m| = 1$ whereas the ω_2 transition has $\Delta m = 0$. This yields some distinct constraints on polarisation and beam propagation direction for each transition, along with particular advantages due to the selection rules.

Coupling strengths Using Wigner-Eckart theorem, it can be shown that the expressions for the relative coupling strengths $g^{(0)}$ and $g^{(\pm1)}$ for $|\Delta m| = 0, 1$ read

$$g^{(0)} = \frac{1}{2}|\cos\gamma \sin 2\phi| \tag{2.1}$$

$$g^{(\pm1)} = \frac{1}{\sqrt{6}}|\cos\gamma \cos 2\phi + i \sin\gamma \cos\phi| \tag{2.2}$$

in terms of γ - the angle between polarisation and the magnetic field and ϕ - the angle between polarisation and the laser beam. The detailed derivation can be found in [19]. These relative coupling strengths are plotted in Figure 2.2.

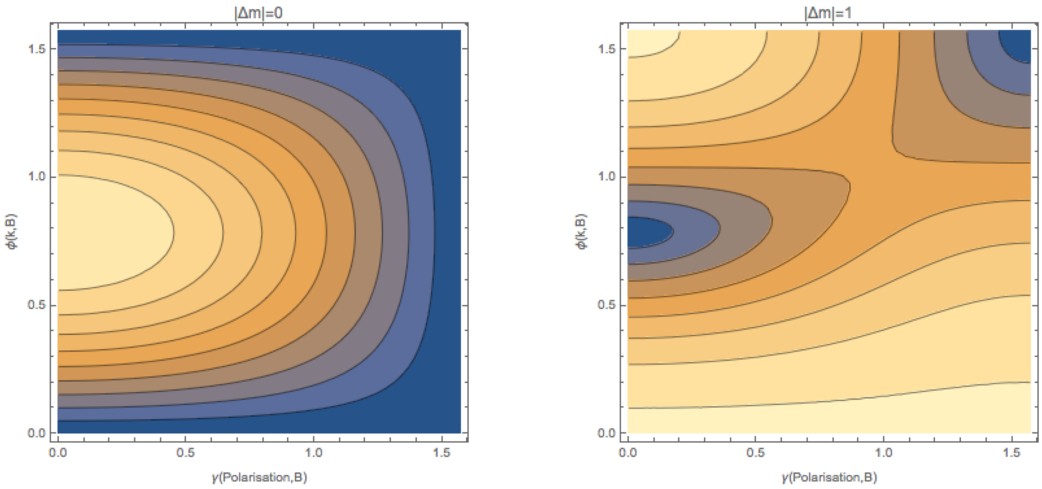

Figure 2.2: Relative coupling strengths on the $S_{1/2} \leftrightarrow D_{5/2}$ for $|\Delta m| = 0, 1$. γ is the angle between polarisation and the magnetic field whereas ϕ is the angle between polarisation and the laser beam, both in radians. Lighter colour indicates higher coupling strength.

It can be seen from the right plot in Figure 2.2 that for the currently accessible transition with frequency ω_1 and $|\Delta m| = 1$, the suitable condition is $\gamma = 0$, so that for a laser beam parallel to the magnetic field, the coupling strength is maximised regardless of the polarisation of the light.

On the other hand, for ω_2 transition with $\Delta m = 0$, the constraint is more strict. The left plot in Figure 2.2 indicates that $\Delta m = 0$ transitions are excited most strongly when $\phi = 45°, \gamma = 0°$. The selection rules prevent the $|\Delta m| = 1$ transitions to couple to the laser in this configuration. This can clearly be seen by observing the overlapping light and dark coloured $\phi \approx 45°, \gamma \approx 0°$ regions of $\Delta m = 0$ and $|\Delta m| = 1$ plots in Figure 2.2. Another advantage of this transition is that the resonance frequency ω_2 is robust against magnetic field fluctuations, so that a field fluctuation of $\Delta B = 1$ mG shifts the resonance frequency by only 550 Hz [20].

Another transition which is less relevant to this thesis is the 397 nm transition which is used for Doppler cooling and state detection.

2.2 Setup Background

2.2.1 Acousto-optic Modulators (AOM)

It is a well known phenomenon that light that is incident on gradients of refractive index is scattered. AOM's principle of operation is based on this fact: the incident light is scattered by the acoustic wavefronts due to periodic pressure variations in a nonlinear medium due to travelling sound waves generated by a piezoelectric transducer. In an AOM, the energy of the scattered light shifts and the light gets deflected due to a shift in its momentum.

From the perspective of condensed matter physics, both the energy and momentum shifts are explained in terms of phonon-photon interactions. When the photon of frequency ω is incident to the phonons of frequency Ω corresponding to matter waves in the AOM media, the 0 order corresponds to no interaction, $+1$ order corresponds to an anti-Stokes process (in a loose language, absorption of a phonon by a photon.) and -1 order corresponds to a Stokes process (similarly, emission of phonon by the incident photon). As a result, $+1$ order light is shifted by $+\Omega$ in energy likewise -1 order is shifted by $-\Omega$.

Another perspective suggests that if we use a toy model, ignore the fact that the acoustic wavefronts are travelling and assume that the light of wavelength λ[2] is scattered from standing acoustic waves of wavelength Λ; then the phenomenon of deflection is explained by Bragg condition for constructive interference of light scattered from a lattice

$$m\lambda = 2\Lambda \sin\theta_d \tag{2.3}$$

where integer m is the order of diffraction and θ_d is half the angle of deflection which in this case is equal to the angle of incidence to conserve energy and momentum. If we further assume that both acoustic and optical wavefronts are plane waves, then the Bragg condition allows only one value of deflection angle $\Theta = 2\theta$. However in the realistic case of acoustic waves with wavefronts of finite curvature, the Bragg condition with certain m (e.g. $m = 1$ in Figure 2.3.a) results in scattering of some light with angle $n\Theta$, n corresponding to other orders of diffraction [21]. This is illustrated in Figure 2.3.b.

[2]Note that there is a subtle difference between the operation principle of AOMs used for different wavelengths: The AOMs for the near infrared light are polarization insensitive, whereas in the UV regime the diffraction efficiency strongly depends on the polarization of the incoming beam.

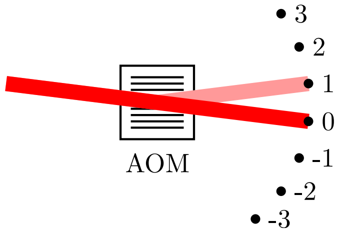

(a) Light scattering from ideal infinitely wide acoustic waves in an AOM.

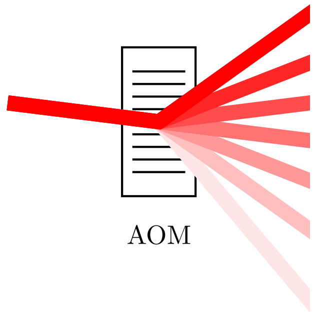

(b) The finite width of the acoustic waves in an AOM results in weak scattering of light to other orders in addition to what Bragg condition implies.

Figure 2.3: The deflection of light due to momentum shifting in an AOM.

On the other hand, the shift in the energy that the deflected beams acquire cannot be explained by this simplified standing acoustic wave model. It is important to note that as opposed to Bragg scattering, in AOMs, the light is scattering from travelling plane waves. The realistic model of interaction of light and travelling material waves within a medium is called Brillouin scattering. From the classical point of view, since the "acoustic crystal" that diffracts the beam is travelling, the frequency of the diffracted beam in order n will be Doppler-shifted by an amount equal to the frequency of the sound wave. This corresponds to the Brillouin shift in the energy.

2.2.2 PDH lock

Locking a laser to an etalon provides a reference for the frequency and stabilizes the frequency of the laser.

In addition to the condition $2L = n\lambda$ for the wavelength of laser beam λ and the cavity length L for an integer n, in order to lock a laser beam to a cavity, the radii of curvature of the cavity mirrors have to match the radii of curvature of the wavefronts of the Gaussian beam at both positions where the mirrors are placed. Experimentally, the cavity length is tuned by piezoelectric elements until the reflection coefficient is measured to be 0 in the case of resonance. In principle, this direct method should work. However, real part of reflection coefficient $F(\omega)$ has symmetric peaks, hence the reflection measurements do not tell about the sign of frequency shift.

To overcome this problem, Pound, Drever and Hall proposed the PDH scheme. Light from the laser is modulated by generating two equally spaced (blue and red) sidebands which are far off resonance with respect to the reference cavity with free spectral range FSR by an electro-optic modulator (EOM) driven by a local oscillator, and sent into the reference cavity. The light reflected from the reference cavity is detected by a high frequency photodiode. The output signal is mixed with the signal from the local oscillator before being low-pass filtered. This yields an anti-symmetric error signal that indicates the sign of the frequency shift. The interested reader is directed to reference [22] for more details.

The cavity in the B18 laboratory has a free spectral range is about $|\Delta\nu_{FSR}| = 1.5$ GHz. In the current lock, the 729 nm laser is locked to ω =411.0427 THz and the transmitted power is about 10 µW - 20 µW. Increased laser power is desired in order to achieve larger Rabi frequencies.

2.3 Experimental Setup

To explain why the +1 order diffraction is chosen for the AOM double-pass configuration, it would be helpful to consider the full laser setup in the B18 laboratory.

The setup in the B18 includes two main elements that alter the frequency of the incident 729 nm beam generated by the source. This is illustrated in Figure 2.4. Firstly, the laser is PDH locked into a reference cavity. There, the frequency can be altered by an amount of one free spectral range (FSR) locking the laser beam to the upper or the lower fringe. Note that the $\Delta\nu_{FSR} = \pm 1.5$ GHz for the B18 cavity. The lock acts on the laser current and thus the transmitted light has a narrow linewidth, as well. Afterwards the beam passes through our AOM setup in double-pass configuration and the frequency shifts by $2\Omega_{AOM} = \pm 400$ MHz.

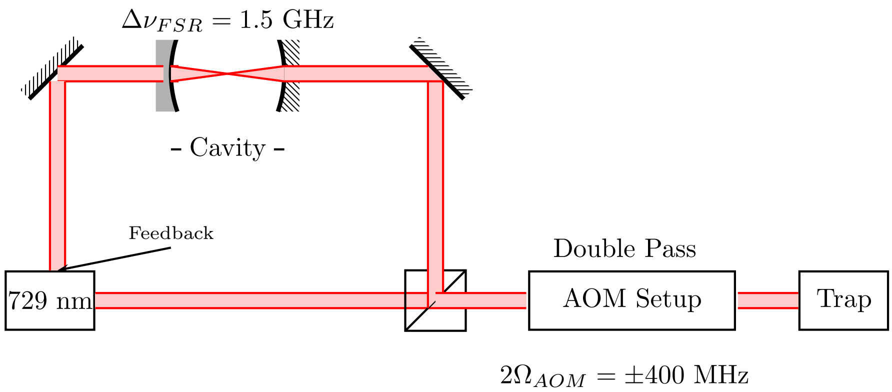

Figure 2.4: A simplified scheme of the experimental setup in the B18 lab.

As mentioned previously, the current setup in the B20 laboratory is able to address the $|^2S_{1/2}, m_J = +1/2\rangle \leftrightarrow |^2D_{5/2}, m_J = -1/2\rangle$ transition with frequency ω_1 (see Figure 2.1). If we denote the cavity locked laser frequency in the B20 setup by ω_{B20}, this is related to the transition frequency as $\omega_1 = \omega_{B20} - 700$ MHz [23]. Since the frequency difference between the two $^2S_{1/2}$ levels is 315 MHz, it is immediately deduced that $\omega_2 = \omega_{B20} - 385$ MHz (see Figure 2.1). Furthermore, the B18 laser centre frequency ω_{B18} is related to ω_{B20} as $\omega_{B18} = \omega_{B20} + 700$ MHz [23].

In order to achieve the transition frequency ω_2 by the B18 setup, the necessary condition is

$$\omega_2 = \omega_{B18} + \Delta\nu_{FSR} + 2\Omega_{AOM} \tag{2.4}$$

which is simplified by using the relationships that are given above;

$$\Delta\nu_{FSR} + 2\Omega_{AOM} = -1.085 \text{ GHz} \tag{2.5}$$

Equation (2.5) is satisfied when the B18 729 nm laser is locked to the lower fringe instead of the centre frequency, that is $\Delta\nu_{FSR} = -1.5$ GHz and the +1 order diffraction is taken from the AOM setup, i.e. $2\Omega_{AOM} = +400$ MHz.

2.3.1 AOM double-pass Configuration

In our setup, the AOM is used in the double-pass configuration. Once a laser beam passes through an AOM, reflecting this beam back towards the AOM allows for doubling the frequency shift whilst the double pass configuration ensures that the angle of incidence within the setup does not depend on Bragg refraction, so that all the mirrors in the optical setup remain in the correct angle for the back reflected beam [24].

More precisely, in the double-pass configuration, a beam with frequency ω_i first enters the AOM to be diffracted to the ± 1 order. The zeroth order is blocked by an aperture. Then the ± 1 order beam is reflected by a mirror back onto itself and then passes back through the AOM. Another aperture blocks the zeroth order and only the beam which is diffracted in the ± 1 is allowed to pass through[3]. The resulting beam has a frequency $\omega_f = \omega_i \pm 2\Omega_{AOM}$ and it has no deflection with respect to the incident beam.

Breadboard Design

The breadboard design for the AOM setup is presented schematically in Figure 2.5. To progress with the description of the design, we are aided by this figure.

[3]Note that the order sign of first order diffraction for each first and the second pass should be the same in order to double the frequency shift. Otherwise, obviously, no frequency shift occurs.

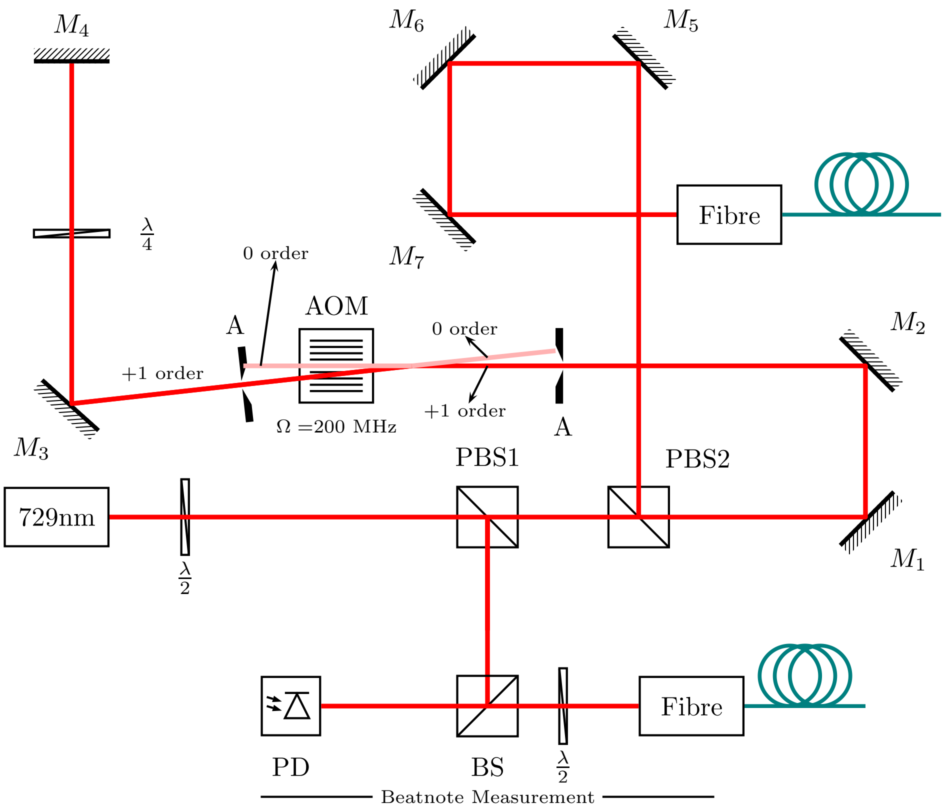

Figure 2.5: Frequency modulation scheme with an AOM in double-pass configuration. The top right part is concerned with fibre-coupling and the bottom right part represents the beatnote measurement.

To illustrate the design, the setup can be examined component by component. Firstly, the beam generated by the 729 nm source (with the corresponding frequency $\omega \approx 411$ THz) passes through a half wave plate (HWP). HWP rotates the polarisation of the incident beam. The first polarising beam splitter (PBS1) allows a component of the rotated beam with linear polarisation **P** to pass through and the reflected beam goes to the beatnote measurement. The second polarising beam splitter (PBS2) is ineffective at the first pass, i.e. beam passes through it without reflection. Then this linearly polarised beam double-passes through the AOM with acoustic frequency $\Omega_{AOM} = 200$ MHz[4] as it is back reflected by the mirror M_4. The two apertures are placed in

[4]The AOM is fed by an RF supply that is connected through an amplifier and an RF synthesizer. For further details, please see Section 2.4.1.

such a way that only the +1 order diffraction is allowed to pass each time[5]. Meanwhile the beam also passes through the quarter wave-plate twice, so that the direction of its linear polarisation is rotated by 90 degrees.

Therefore, the beam gains a polarisation $\mathbf{P}'$ perpendicular to $\mathbf{P}$ and frequency $\omega' = \omega + 2\Omega_{AOM}$. As a result of this altered polarisation, the back-reflected beam is separated from the incoming beam as it is fully reflected by PBS2 towards fiber coupling as illustrated on the top right corner of Figure 2.5.

2.4 Setup Characterisation

2.4.1 AOM Efficiency Characterisation

To characterise the AOM, the dependence of transmitted optical power efficiency on frequency and the the input RF power is measured for the 200 MHz IntraAction AOM[6] for in both single and double pass configurations. The efficiency is determined by the ratio of the total incoming power and the transmitted first order power, which are both measured by a power meter. It has been found that in the optimal case, the efficiency in optical power at the single pass is 75% and the efficiency at the double-pass is 56%.

RF Synthesizer Centre Frequency

The plot of the frequency dependence of AOM single and double-pass efficiencies are given in Figure 2.6. This data is taken by scanning through frequencies between 190 MHz and 210 MHz by steps of 500 kHz on the RF synthesizer with fixed input power of 30 dBm.

[5] See Section 2.3 for the reasoning of the choice of +1 order diffraction.

[6] Model: IntraAction Corp. Acousto-Optics ATM - 2001A2.

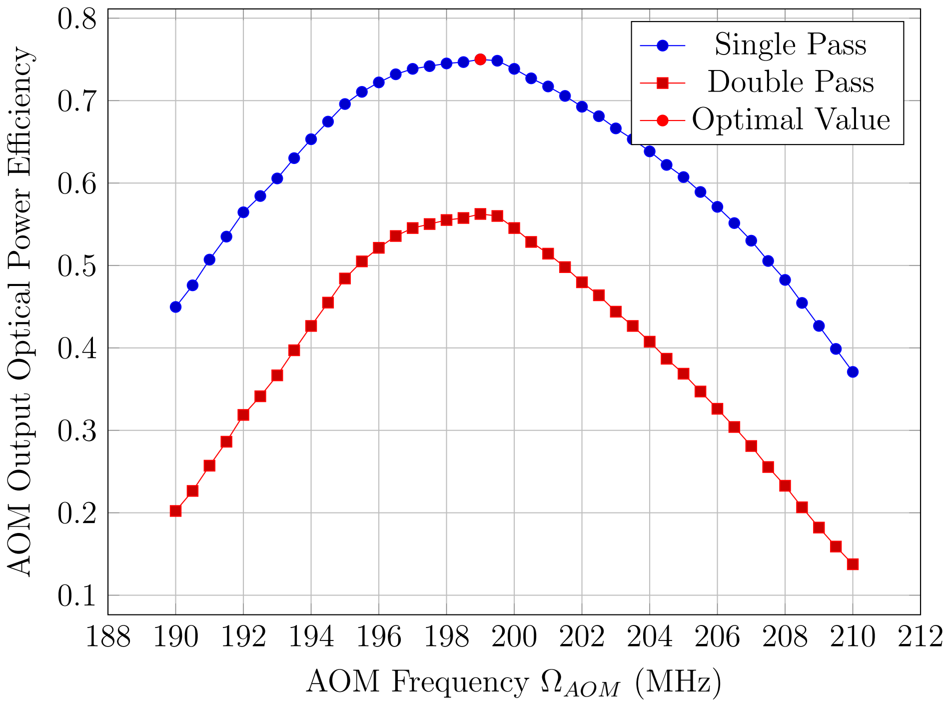

Figure 2.6: Comparison of measured AOM single-pass (blue circles) and double-pass (red squares) efficiencies. The double-pass values are approximately the square of the single-pass values.

The data presented in Figure 2.6 indicates that the optimal frequency for the AOM slightly deviates from 200 MHz and it is around 199 MHz.

AOM Input Power

In an analogous manner, the optimal RF power for the AOM is determined by stepping the RF power by intervals of 1 dBm within the range 23 dBm and 30 dBm for the fixed frequency equal to the optimal value 199 MHz. The measurement has been taken in the single-pass and the data is plotted in Figure 2.7.

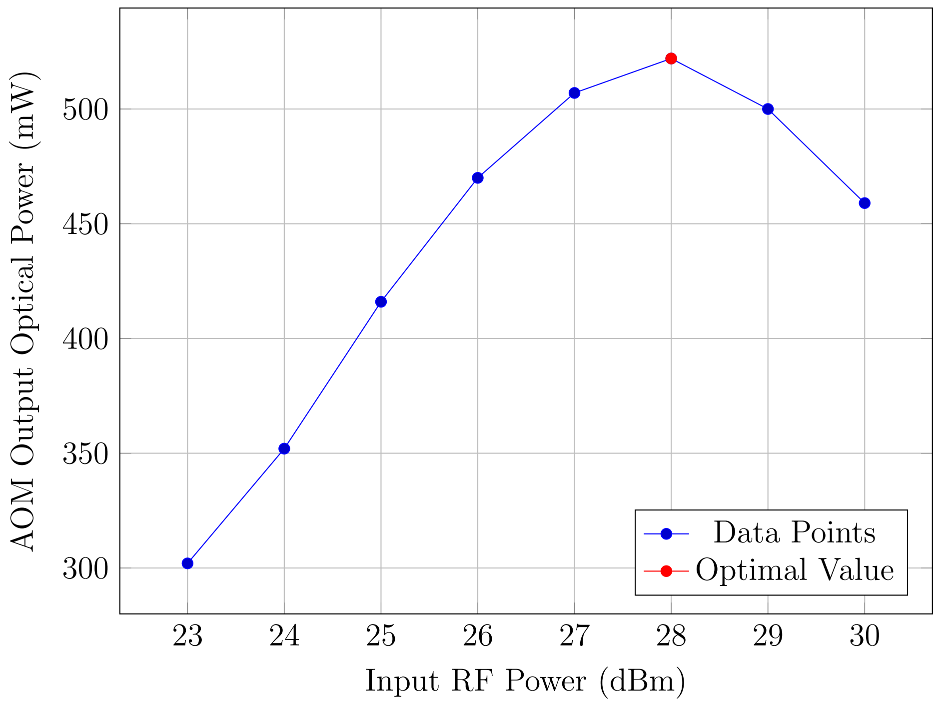

Figure 2.7: The dependence of AOM transmitted optical power on the RF power in the single-pass configuration.

As indicated in Figure 2.7, the optimal input power is determined to be 28 dBm. This is achieved by using 7 dBm attenuators on the output channel of the RF synthesizer.

In the experiments, the AOM frequency is controlled by direct digital synthesizers (DDS) that are fed into an RF amplifier. The DDS is calibrated in a way that the AOM output optical power is maintained whilst the frequency is tuned within a specific range [25].

2.5 Conclusion

This chapter of the thesis briefly introduces the thermodynamics experiment protocol that the AOM setup that is built is going to be utilised for. The prospect of realising an ionic Szilard's engine is discussed briefly. The protocol comprises the $^{40}Ca^+$ ion as the thermal qubit.

The $^{40}Ca^+$ transitions that are required to be addressed by the experimental setup are mentioned in Chapter 2.1.1. The designed system is able to generate light in the frequency of the currently inaccessible $|^2S_{1/2}, m_J = -1/2\rangle \leftrightarrow |^2D_{5/2}, m_J = -1/2\rangle$ transition by altering frequency of the PDH locked laser by +400MHz using a double-passed 200MHz AOM. The setup design is described in Chapter 2.3.

The single-pass and double-pass optical power efficiencies of the setup that is constructed are measured to be 75% and 56%, respectively. These values are optimised by using the correct input power and frequency values which are determined after AOM characterisation, discussed in Chapter 2.4.

Addressing the $|^2S_{1/2}, m_J = -1/2\rangle \leftrightarrow |^2D_{5/2}, m_J = -1/2\rangle$ transition in $^{40}\mathrm{Ca}^+$ is an important step towards realising the proposed experimental protocol, since the other relevant transitions are already accessible with the current setup.

Bibliography

[1] C. Monroe and J. Kim. “Scaling the Ion Trap Quantum Processor”. In: *Science* 339.6124 (2013), pp. 1164–1169. ISSN: 0036-8075. DOI: 10.1126/science.1231298.

[2] Rainer Blatt and Christian F Roos. “Quantum simulations with trapped ions”. In: *Nature Physics* 8.4 (2012), p. 277.

[3] Wolfgang Paul. “Electromagnetic traps for charged and neutral particles”. In: *Reviews of modern physics* 62.3 (1990), p. 531.

[4] Hartmut Häffner, Christian F Roos, and Rainer Blatt. “Quantum computing with trapped ions”. In: *Physics reports* 469.4 (2008), pp. 155–203.

[5] Jürgen Eschner et al. “Laser cooling of trapped ions”. In: *JOSA B* 20.5 (2003), pp. 1003–1015.

[6] Juan I Cirac and Peter Zoller. “Quantum computations with cold trapped ions”. In: *Physical review letters* 74.20 (1995), p. 4091.

[7] Kenneth R Brown, Jungsang Kim, and Christopher Monroe. “Co-designing a scalable quantum computer with trapped atomic ions”. In: *arXiv preprint arXiv:1602.02840* (2016).

[8] JP Home. “Quantum science and metrology with mixed-species ion chains, 2013”. In: *arXiv preprint arXiv:1306.5950* ().

[9] Ting Rei Tan et al. “Multi-element logic gates for trapped-ion qubits”. In: *Nature* 528.7582 (2015), pp. 380–383.

[10] Daniel Kienzler. “Quantum Harmonic Oscillator State Synthesis by Reservoir Engineering”. PhD thesis. ETH Zürich, 2015.

[11] David B Hume. “Two-species ion arrays for quantum logic spectroscopy and entanglement generation”. PhD thesis. University of Colorado at Boulder, 2010.

[12] Murray D Barrett et al. “Sympathetic cooling of 9 Be+ and 24 Mg+ for quantum logic”. In: *Physical Review A* 68.4 (2003), p. 042302.

[13] DJ Larson et al. “Sympathetic cooling of trapped ions: A laser-cooled two-species nonneutral ion plasma”. In: *Physical review letters* 57.1 (1986), p. 70.

[14] Sidney A Self. “Focusing of spherical Gaussian beams”. In: *Applied optics* 22.5 (1983), pp. 658–661.

[15] William H Carter. “Focal shift and concept of effective Fresnel number for a Gaussian laser beam”. In: *Applied optics* 21.11 (1982), pp. 1989–1994.

[16] H.D. Taylor. *taylor*. US Patent 540,122. May 1895. URL: `https://www.google.ch/patents/US540122`.

[17] Thorlabs Inc. *Product Raw Data for Uncoated UVFS, 10mm Thick Sample*. 2017. URL: `https://www.thorlabs.com/images/TabImages/Uncoated_UVFS_Transmission.xlsx`.

[18] HC Nägerl et al. “Investigating a qubit candidate: Spectroscopy on the S 1/2 to D 5/2 transition of a trapped calcium ion in a linear Paul trap”. In: *Physical Review A* 61.2 (2000), p. 023405.

[19] Daniel FV James. “Quantum dynamics of cold trapped ions with application to quantum computation”. In: *Applied Physics B: Lasers and Optics* 66.2 (1998), pp. 181–190.

[20] Christian Roos. “Controlling the quantum state of trapped ions”. In: (2000).

[21] DJ McCarron. *A guide to acousto-optic modulators*. Tech. rep. Technical report, Durham University, 2007.

[22] Eric D Black. “An introduction to Pound–Drever–Hall laser frequency stabilization”. In: *American Journal of Physics* 69.1 (2001), pp. 79–87.

[23] Christa Flühmann. “Stabilizing lasers and magnetic fields for quantum information experiments”. MA thesis. ETH Zürich, 2014.

[24] EA Donley et al. “Double-pass acousto-optic modulator system”. In: *Review of Scientific Instruments* 76.6 (2005), p. 063112.

[25] Karin Fisher. “Coherent Control Laser System for the Quantum State Manipulation of Trapped Ions”. MA thesis. ETH Zürich, 2013.